Received: 3 March 2020 | Revised: 1 July 2020 | Accepted: 16 July 2020

DOI: 10.1002/mrm.28468

FULL PAPER

Magnetic Resonance in Medicine

Adaptive slice-specific z-shimming for 2D spoiled gradient-echo sequences

Martin Soellradl[1] | Johannes Strasser[1] | Andreas Lesch[2] | Rudolf Stollberger[2] | Stefan Ropele[1] | Christian Langkammer[1]

[1]Department of Neurology, Medical University of Graz, Graz, Austria

[2]Institute of Medical Engineering, Graz University of Technology, Graz, Austria

Correspondence
Martin Soellradl, Department of Neurology, Medical University of Graz, Graz, Austria.
Email: martin.soellradl@medunigraz.at

Funding information
Austrian Science Fund, Grant/Award Number: KLI 523 and P 30134

Purpose: To reduce the misbalance between compensation gradients and macroscopic field gradients, we introduce an adaptive slice-specific z-shimming approach for 2D spoiled multi-echo gradient-echoe sequences in combination with modeling of the signal decay.

Methods: Macroscopic field gradients were estimated for each slice from a fast prescan (15 seconds) and then used to calculate slice-specific compensation moments along the echo train. The coverage of the compensated field gradients was increased by applying three positive and three negative moments. With a forward model, which considered the effect of the slice profile, the z-shim moment, and the field gradient, R_2^* maps were estimated. The method was evaluated in phantom and in vivo measurements at 3 T and compared with a spoiled multi-echo gradient-echo and a global z-shimming approach without slice-specific compensation.

Results: The proposed method yielded higher SNR in R_2^* maps due to a broader range of compensated macroscopic field gradients compared with global z-shimming. In global white matter, the mean interquartile range, proxy for SNR, could be decreased to 3.06 s^{-1} with the proposed approach, compared with 3.37 s^{-1} for global z-shimming and 3.52 s^{-1} for uncompensated multi-echo gradient-echo.

Conclusion: Adaptive slice-specific compensation gradients between echoes substantially improved the SNR of R_2^* maps, and the signal could also be rephased in anatomical areas, where it has already been completely dephased.

KEYWORDS
field inhomogeneities, gradient-echo, R_2^* relaxometry, T_2^* relaxometry, z-shim

1 | INTRODUCTION

Magnetic resonance imaging sequences based on gradient-echo (GRE) readout strategies play a major role in clinical routine, and because of their low specific absorption rate behavior, they are used increasingly at ultrahigh field strengths. Besides the morphological information provided by GRE images, the decay of the complex signal offers insights into the underlying tissue compartments and their susceptibilities.[1-11] Over the entire physiological range, the

This is an open access article under the terms of the Creative Commons Attribution License, which permits use, distribution and reproduction in any medium, provided the original work is properly cited.
© 2020 The Authors. *Magnetic Resonance in Medicine* published by Wiley Periodicals LLC on behalf of International Society for Magnetic Resonance in Medicine

effective transverse relaxation rate R_2^* serves as a proxy for iron concentration and has been used to study inflammatory and degenerative diseases in the brain,[12,13] iron overload in the liver,[14] and myocardial iron overload.[15]

However, obtaining quantitative R_2^* values from gradient-echoes is typically subject to quantification errors due to faster intravoxel dephasing caused by macroscopic field variations[16] (such as near air/tissue interfaces). In 2D spoiled GRE imaging, dephasing is more pronounced along the slice direction because the slice thickness is usually much larger than the in-plane resolution. Consequently, an effective approach to reduce signal dephasing is to decrease the slice thickness, which is accompanied by reduced SNR and prolonged acquisition time.[17] Various postprocessing methods for reducing these dephasing effects by considering the slice profile and macroscopic field variations have been proposed,[18-23] but at very strong field gradients the correction of the fast signal decay might not be feasible.

Alternatively, z-shimming approaches allow compensating signal dephasing due to a certain macroscopic field gradient G_z by variation of the compensation gradient moment in the slice-selective direction. Starting from the basic principle of changing the amplitude of the slice-selective refocusing gradient demonstrated by Frahm et al,[24] different methods have evolved. To minimize the effects of G_z on T_2' quantification, Ordidge et al proposed the acquisition of images with different refocusing gradients.[25] Similarly, the GRE slice excitation profile imaging method acquires several images with an equidistant spacing of compensation gradients to estimate the k-space shift in z-direction, which allows reconstruction of a magnitude image with minimal contribution of G_z.[26] The method was applied to R_2^* mapping,[27] and by adding compensation gradients between the echo acquisitions, a more efficient sampling is possible.[28] Nonetheless, a drawback of these approaches is that several additional images need to be acquired, which limits their application in clinical routine because of the prolonged scan time.

Similarly, Meng et al started with one strong compensation gradient before acquiring the echo train and successively rephased it with small opposed inter-echo gradients.[29] To reduce acquisition time, Wild et al proposed a single-scan method by applying repetitively a triple of compensation gradients between echo acquisition of a spoiled multi-echo GRE sequence (mGRE).[30] However, all of these methods assume an ideal slice profile, which would give rise to a sinc-shaped signal decay in the presence of G_z.[16] Addressing variations of slice profile, Nam et al proposed a single-scan z-shim approach that includes the slice profile and compensates for a positive and negative G_z by applying compensation gradients that are linearly scaled with TE.[31] To avoid signal crushing of the first echoes, Lee et al started the z-shim after the fifth echo for myelin water signal mapping.[32]

A common limitation of the aforementioned approaches is that the compensation gradients are fixed for the entire FOV (global z-shim), and, consequently, a misbalance with the actual field gradient results in incomplete rephasing or even spoiling of the signal.

We therefore propose an adaptive slice-specific z-shimming approach to address spatial variations of G_z. The corresponding slice-specific compensation gradients are estimated for each slice individually from a fast prescan. Additionally, a more effective z-shim pattern is introduced, in which six G_z values are successively compensated between echo acquisitions. By adapting a signal modeling approach for 2D spoiled mGRE sequences,[23] we compare this novel approach, in terms of R_2^* mapping, with a global z-shim approach with linearly increasing moments[31,32] and a conventional mGRE sequence without z-shim gradients. Furthermore, to highlight the importance of adequate signal modeling in the presence of G_z, R_2^* is also estimated from the conventional mGRE data with a more widespread used mono-exponential signal model.

2 | METHODS

2.1 | Signal modeling

Signal dephasing due to a field gradient G_z can be compensated at a TE by applying a short compensation gradient with duration t_c and amplitude G_c, which results in a compensation moment $m_c = G_c t_c = -G_z TE$. In the case of a train of k compensation gradients, each with the amplitude $G_c[k]$ and identical t_c, the accumulative moment $M_c[i]$ for the ith echo at TE_i is given by:

$$M_c[i] = \sum_{k=1}^{i} m_c[k] = \sum_{k=1}^{i} G_c[k]\, t_c = \overline{G}_c[i]\, TE_i. \qquad (1)$$

The sum of all applied compensation moments $m_c[k]$ until TE_i is equal to a single theoretical mean compensation gradient $\overline{G}_c[i]$ applied over the entire duration TE_i. This allows us to superimpose G_z and $\overline{G}_c[i]$ for signal modeling independent of the shape and duration of the applied compensation gradients. Assuming a mono-exponential signal decay with R_2^*, the signal $S(TE_i)$ of the spoiled gradient echo is given by integrating the complex transverse magnetization $\underline{M}_{xy}(z)$ weighted with the phase dispersion induced by both gradients along the z-direction:

$$\begin{aligned} S(TE_i) &= S_0 e^{-R_2^* TE_i} \int_{-\infty}^{\infty} \underline{M}_{xy}(z)\, e^{i\gamma(G_z + \overline{G}_c[i])zTE_i} dz \\ &= S_0 e^{-R_2^* TE_i} F_{z-shim}(TE_i) \end{aligned} \qquad (2)$$

where S_0 describes the signal $S(TE=0)$, and $F_{z-shim}(TE_i)$ summarizes the net effect of G_z and $\overline{G}_c[i]$. In the case of small flip angles, the resulting signal decay is described by the pulse envelope of the RF excitation pulse.[20] Otherwise, the integral in Equation 2 can be solved numerically, where $\underline{M}_{xy}(z)$ is obtained by the numerical solution of the Bloch equations.[22,23]

2.2 | Sequence

Figure 1 shows a 2D spoiled mGRE sequence (Figure 1A) and a combination of the global z-shim patterns proposed by Nam et al and Lee et al[31,32] (Figure 1B) along with the proposed slice-specific pattern presented in this work (Figure 1C). In addition, Table 1 lists the corresponding compensation gradients $\overline{G}_c[i]$ for the z-shim approaches for each echo.

The compensation moments for the global z-shim method (Figure 1B) are calculated for a single positive $\overline{G}_c^+$ and negative $\overline{G}_c^-$ value. The first applied gradient moment after the fourth echo ($m_c[5]=\overline{G}_c^+ TE_5=-G_z^- TE_5$) compensates for the effects of negative G_z^- followed by nulling the accumulative moment by inverting $m_c[5]$ ($m_c[6]=-m_c[5]$). This step is repeated for a positive G_z^+ by applying a negative compensation moment ($m_c[7]=\overline{G}_c^- TE_7=-G_z^+ TE_7$). To avoid crushing of the signal in the first echoes, z-shim gradients are not applied for the first echoes as proposed by Lee et al.[32]

Our work extends the compensation pattern in Figure 1B by two novel contributions. First, instead of using global $\overline{G}_c^{+/-}$ for all slices, slice-specific compensation gradients $\overline{G}_c^{+/-}[n]$ are applied for each slice n. These $\overline{G}_c^{+/-}[n]$ values are estimated from a field map measured with a fast prescan. Second, instead of a single $\overline{G}_c^+[n]$ and $\overline{G}_c^-[n]$, the coverage of compensated $G_z^{+/-}$ values is increased by a successive application of three positive and three negative compensation moments. Based on the estimated $\overline{G}_c^{+/-}[n]$, the moments between echoes are scaled such that $\left[\frac{1}{3},\frac{2}{3},\frac{3}{3}\right]\overline{G}_c^{+/-}[n]$ are compensated for three consecutive echoes, which is followed by a nulling of the total moment for the subsequent echo. To give an example, the moments $m_c[n,5]$ to $m_c[n,7]$ in the proposed pattern (Figure 1C) are calculated as follows, assuming equal echo spacing ΔTE:

$$m_c[n,5]=\frac{1}{3}\overline{G}_c^+[n]\,TE_5 \tag{3}$$

$$m_c[n,6]=\overline{G}_c^+[n]\left(\frac{1}{3}TE_5+\frac{2}{3}\Delta TE\right) \tag{4}$$

$$m_c[n,7]=\overline{G}_c^+[n]\left(\frac{1}{3}TE_5+\frac{4}{3}\Delta TE\right) \tag{5}$$

Moreover, to allow a more effective rephasing, the nonzero value is split into $\left[\frac{1}{5},\frac{2}{5},\frac{3}{5},\frac{4}{5},\frac{5}{5}\right]\overline{G}_c^+[n]$ or

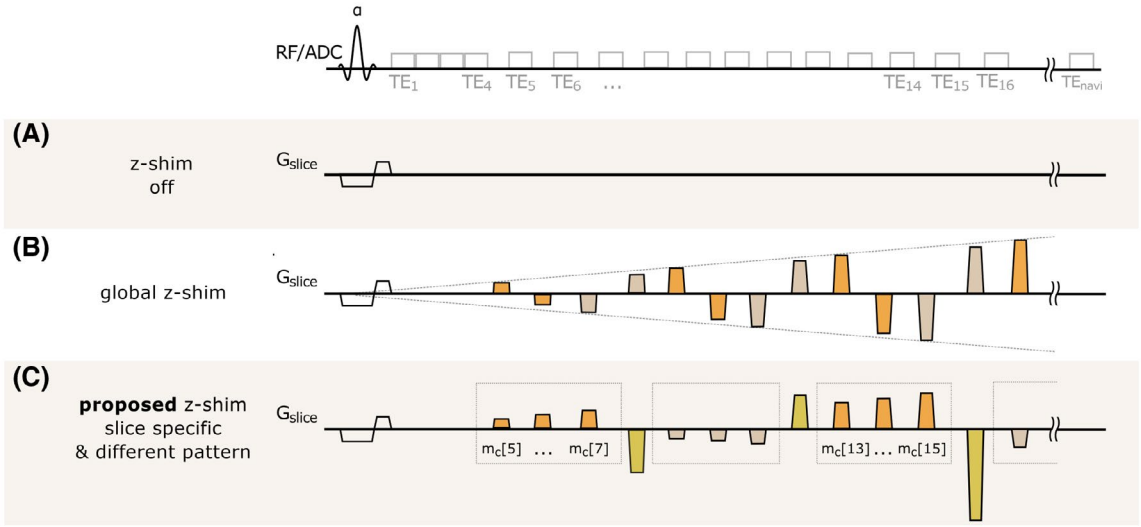

FIGURE 1 Schematic overview of the compared sequences. A, Spoiled multi-echo gradient-echo (mGRE) sequence without z-shimming. B, In the global z-shim approach, moments are applied through alternating pairs (same color) with a linear increase along TE. The first moment in each pair is calculated based on a single positive or negative $\overline{G}_c^{+/-}$, and the second moment balances the compensation moment to acquire a gradient-echo (GRE) image with zero net moment. C, The proposed slice-specific approach, with $\overline{G}_c^{+/-}[n]$ estimated from a prescan individually for each slice n. In addition, $\overline{G}_c^{+/-}[n]$ is split up with factors $\left[\frac{1}{3},\frac{2}{3},\frac{3}{3}\right]\overline{G}_c^{+/-}[n]$ (dashed boxes) followed by compensation of all moments. To correct for physiological fluctuations, a navigator echo is acquired at TE_{navi}

TABLE 1 Mean compensation gradients $\overline{G}_c[i]$ (based on Equation 2) for the global and the proposed z-shim approaches as a function of echo number i

Echo i		1	…	4	5	6	7	8	9	10	11	12	13	14
Global z-shim	$\overline{G}_c^+, \overline{G}_c^-$	0	…	0	$\overline{G}_c^+$	0	$\overline{G}_c^-$	0	$\overline{G}_c^+$	0	$\overline{G}_c^-$	0	$\overline{G}_c^+$	…
Proposed z-shim	$\overline{G}_c^+[n]\neq 0$, $\overline{G}_c^-[n]\neq 0$	0	…	0	$\frac{1}{3}\overline{G}_c^+[n]$	$\frac{2}{3}\overline{G}_c^+[n]$	$\frac{3}{3}\overline{G}_c^+[n]$	0	$\frac{1}{3}\overline{G}_c^-[n]$	$\frac{2}{3}\overline{G}_c^-[n]$	$\frac{3}{3}\overline{G}_c^-[n]$	0	$\frac{1}{3}\overline{G}_c^+[n]$	…
	$\overline{G}_c^-[n]=0$	0	…	0	$\frac{1}{5}\overline{G}_c^+[n]$	$\frac{2}{5}\overline{G}_c^+[n]$	$\frac{3}{5}\overline{G}_c^+[n]$	$\frac{4}{5}\overline{G}_c^+[n]$	$\frac{5}{5}\overline{G}_c^+[n]$	0	$\frac{1}{5}\overline{G}_c^+[n]$	$\frac{2}{5}\overline{G}_c^+[n]$	$\frac{3}{5}\overline{G}_c^+[n]$	…
	$\overline{G}_c^+[n]=0$	0	…	0	$\frac{1}{5}\overline{G}_c^-[n]$	$\frac{2}{5}\overline{G}_c^-[n]$	$\frac{3}{5}\overline{G}_c^-[n]$	$\frac{4}{5}\overline{G}_c^-[n]$	$\frac{5}{5}\overline{G}_c^-[n]$	0	$\frac{1}{5}\overline{G}_c^-[n]$	$\frac{2}{5}\overline{G}_c^-[n]$	$\frac{3}{5}\overline{G}_c^-[n]$	…

Note: Compensation moments in the global z-shim approach are calculated from a single positive $\overline{G}_c^+$ and negative $\overline{G}_c^-$, whereas with the proposed approach, slice-specific values for $\overline{G}_c^+[n]$ and $\overline{G}_c^-[n]$ are estimated for each slice n. To increase coverage of compensated field gradients, these values are divided into three fractions or five fractions in case of $\overline{G}_c^+[n]$ or $\overline{G}_c^-[n]$ is being equal to zero.

$\left[\frac{1}{5}, \frac{2}{5}, \frac{3}{5}, \frac{4}{5}, \frac{5}{5}\right] \overline{G}_c^-[n]$ if either $\overline{G}_c^+[n]$ or $\overline{G}_c^-[n]$ is zero. In addition to the inserted z-shim gradients, for all variants in Figure 1 a navigator echo is acquired after the last echo to compensate for physiologically induced field variations.[33]

2.3 | R_2^* estimation

For all measurements, the complex-valued raw data were first corrected with the phase of the navigator echo as described by Wen et al,[34] followed by a coil combination using the method proposed by Luo et al.[35] Then, $F_{z-shim}(TE_i)$ was calculated as described in Soellradl et al[23] for the model $F_4(t)$. In this model, $\underline{M}_{xy}(z)$ is estimated for a certain RF pulse shape and G_{slice} with a numerical Bloch solver.[36] Additionally, two potential factors that might affect $\underline{M}_{xy}(z)$ were included: first, the nominal flip angle deviations due to the transmit RF field B_1^+ and second, G_z is superimposed with G_{slice}, which leads to a change of the spatial encoding from z to $z' = z\lambda$ with $\lambda = \frac{G_{slice}}{G_z + G_{slice}}$.[37] Thus, depending on the sign and amplitude of G_z, the nominal slice thickness Δz is changed to $\Delta z'$, which is given by $\Delta z' = \Delta z \lambda$.

After the estimation of $\underline{M}_{xy}(z)$, $F_{z-shim}(TE_i)$ was calculated for each echo by substituting $G_{z,input}[i]$ with $G_{z,input}[i] = G_z + \overline{G}_c[i]$ to include the z-shim gradients. Using $F_{z-shim}(TE_i)$, R_2^*, and S_0 were estimated by nonlinear fitting of the reconstructed magnitude data to Equation (2) using the *lsqnonlin()* function in *MATLAB* (MathWorks, Natick, MA).

2.4 | Sequence and model evaluation

The differences between the investigated sequences and the proposed signal modeling were assessed by calculating four different R_2^* maps: From the measured data of all three sequences, R_2^* was estimated with the signal model described previously. Additionally, R_2^* maps were calculated by fitting the standard spoiled mGRE data to a mono-exponential signal decay $\left(S_{mono}(TE_i) = S_0 e^{-R_2^* TE_i}\right)$.

2.5 | Phantom experiments

All experiments were carried out on a whole-body 3T MRI system (Magnetom Prisma; Siemens, Erlangen, Germany) using an eight-channel knee coil. To evaluate the proposed z-shim pattern, a homogenous phantom (5 g/L agar doped with 110 μmol/L Magnevist to shorten T_1) was built. Measurements with a spoiled 2D mGRE (Figure 1A), a global z-shim pattern (Figure 1B), and the proposed slice-specific z-shimming approach (Figure 1C) were performed. To allow a comparison between the acquisition methods for the estimation of R_2^*, all sequence parameters were set identically—except the

amplitudes of the z-shim gradients. A sinc-Hanning windowed RF excitation pulse (pulse duration $T_{pulse} = 2$ ms, time-bandwidth product = 2.7) with flip angle $\alpha = 60°$ was used. In total, 20 echoes with a monopolar readout and a bandwidth = 500 Hz/Px were acquired. The echo spacing was 3.4 ms for the first four echoes without z-shim gradients, starting with $TE_1 = 2.8$ ms up to $TE_4 = 12.9$ ms. For the subsequent echoes with z-shim gradients ($t_c = 2$ ms), the echo spacing was increased to 5.4 ms ($TE_5 = 18.2$ ms to $TE_{20} = 98.8$ ms). After the 20th echo, phase encoding was rewound to acquire a navigator echo at $TE_{navi} = 103.4$ ms. A total of 26 slices with a spatial resolution of $1 \times 1 \times 4$ mm^3 (FOV = 128×128 mm^2) were acquired in an interleaved slice-acquisition scheme with a TR = 3 seconds. For all z-shimming approaches, z-shim gradients were applied with $t_c = 2$ ms starting after the fourth echo. For the measurements with the global z-shim pattern (Figure 1B), $\overline{G}_c^{+/-}$ was set to $\pm 100 \mu T/m$. This value was approximately half of the maximum magnitude of the observed field gradients G_z in the phantom. In addition to the mGRE sequences, a B_1 map was acquired using a Bloch-Siegert approach.[38]

2.6 | Prescan to estimate $\overline{G}_c^{+/-}[n]$

For the proposed z-shim approach, a prescan was done to estimate $\overline{G}_c^{+/-}[n]$. The prescan acquisition was performed with the same slice thickness (4 mm), an in-plane resolution of 2×2 mm^2 (FOV = 64×64 mm^2), three echoes with TE = 2.7 ms, 4.8 ms and 6.9 ms, and GRAPPA acceleration of 2. The phase data of the prescan was then automatically processed to estimate the positive $\overline{G}_c^{+}[n]$ and negative $\overline{G}_c^{-}[n]$ for each slice as follows: The phase data were unwrapped using PRELUDE,[39] and the field map was estimated by dividing the phase difference by the TE difference between the third and first echo. For evaluation, a mask was created by thresholding the magnitude image, which then was eroded with disk elements (radius of 5 pixels) to eliminate outliers close to the border. To estimate the field gradient map $G_{z,pre}$, the gradient in z-direction of the field map was calculated in regions within the mask and smoothed with a 3D Gaussian filter (kernel size of 1). Then, the $G_{z,pre}$ map was quantized with an interval of 10 μT/m. For each slice, $\overline{G}_c^{+}[n]$ was set to the minimum of negative $G_{z,pre}[n]$ values ($\overline{G}_c^{+}[n] = \min(G_{z,pre}[n] < 0)$ and for $\overline{G}_c^{-}[n]$ to the maximum of $G_{z,pre}[n]$ ($\overline{G}_c^{-}[n] = \max(G_{z,pre}[n] > 0)$. Before scanning with the proposed z-shimming approach, the specific interecho compensation moments were calculated based on the pattern listed in Table 1.

2.7 | In vivo experiments

The proposed slice-specific z-shimming approach (Figure 1C) was evaluated for in vivo R_2^* mapping by comparing the results with the global approach (Figure 1B) and the approach without z-shimming (Figure 1A). In total, 3 subjects were scanned on the same 3T MRI system using a 20-channel head coil. The study was approved by the local ethics committee, and all subjects gave written informed consent. For all experiments, the same RF excitation pulse as in the phantom measurements was used. Sixteen echoes and one navigator echo were acquired with $TE_1 = 3$ ms to $TE_4 = 9.7$ ms (without z-shim gradients, echo spacing = 2.2 ms), $TE_5 = 13.9$ ms to $TE_{16} = 60.6$ ms (with z-shim gradients $t_c = 2$ ms, echo spacing = 4.2 ms), and $TE_{navi} = 64.8$ ms. Further sequence parameters included a bipolar readout with bandwidth = 500 Hz/Px, TR = 2.5 seconds, and 35 slices with a voxel size of $1 \times 1 \times 3$ mm^3 (FOV = 256×176 mm^2). As proposed by Nam et al,[31] the value of $\overline{G}_c^{+/-}$ was set to $\pm 220 \frac{\mu T}{m}$ for the global approach. The slice-specific compensation gradients $\overline{G}_c^{+/-}[n]$ were estimated from a prescan as described for the phantom measurements, except that the mask was generated with the brain extraction tool BET, part of FSL.[39] Sequence parameters of the prescan were 35 slices with a voxel size of $2.3 \times 2.3 \times 3$ mm^3 (FOV = 96×78 mm^2), three echoes with TE = 2.7 ms, 4.8 ms and 6.9 ms, and a GRAPPA acceleration factor of 3 with 20 reference lines, TR = 344 ms, $\alpha = 20°$.

The acquisition times were 15 seconds for the prescan and 7 minutes 20 seconds for each of the three GRE sequences. In addition to the mGRE sequences, an MPRAGE sequence with 1-mm^3 isotropic resolution was acquired for anatomical segmentation. Furthermore, B_1 mapping was performed with a highly accelerated approach based on the Bloch-Siegert shift.[40]

The different methods were compared by calculating the median and interquartile range of R_2^* values in global white-matter and gray-matter masks. The global white-matter masks were obtained from MPRAGE images using SIENAX,[41] part of FSL,[39] and subcortical gray-matter masks using FSL FIRST.[42] Regional R_2^* evaluation (median; interquartile range) was performed after affine registration to mGRE space with FSL FLIRT.[43,44]

3 | RESULTS

3.1 | Phantom

Figure 2 shows the signal decay of the three investigated pulse sequences within one slice. To demonstrate effects of varying G_z, three regions of interest (ROIs) (Figure 2B) with different G_z intervals were defined, and their normalized averaged signal decay S_{norm} (Figure 2C) and averaged F_{z-shim} (Figure 2D) were plotted. The standard spoiled mGRE sequence reveals a faster decay of S_{norm} with increasing magnitude of G_z, whereas for the z-shim approaches, S_{norm} is differently rephased or dephased. For the global z-shim,

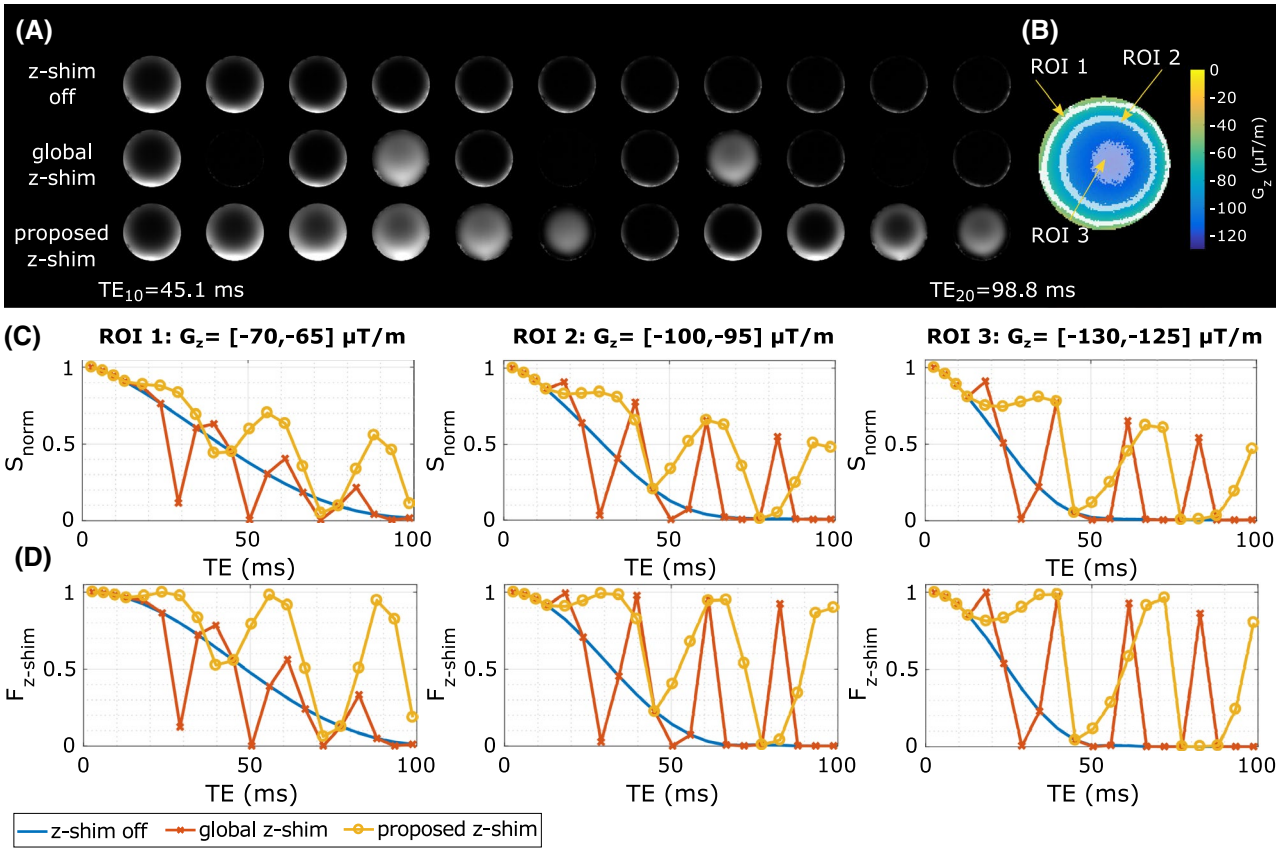

FIGURE 2 Comparison of the measured averaged normalized signal decay $S_{norm}(TE_i) = S(TE_i)/S(TE_1)$ and the estimated dephasing functions $F_{z-shim}(TE_i)$ within one slice. A, The magnitude images of TE_{10} to TE_{20}. B, Regions of interest (ROIs) were defined within different field gradient intervals, G_z. In these ROIs, the $S_{norm}(TE_i)$ (C) and the averaged $F_{z-shim}(TE)$ (D) were estimated. The lines in (C) and (D) show the results from a spoiled mGRE sequence without z-shim gradients in blue, with the global z-shim approach ($|\overline{G_c}^{+/-}| = 100\mu T/m$) in red, and with the proposed slice-specific z-shimming in yellow. Note: The interpolation between echoes is solely for illustration purposes

the best signal rephasing is achieved in ROI 2, where $\overline{G_c}^{+} \approx -G_z = 100\mu\frac{T}{m}$, followed by ROI 3. In ROI 1, on the contrary, with an G_z interval of $G_z = [-70, -65]\,\mu\frac{T}{m}$, only a small portion of the signal is rephased. In contrast to the global z-shim, the prescan-estimated compensation gradients for the proposed approach were $\overline{G_c}^{+}[n=4] = 125\mu\frac{T}{m}$ and $\overline{G_c}^{-}[n=4] = 0$. Thus, only positive compensation gradients were applied in five fractions ($[25, 50, 75, 100, 125]\,\mu\frac{T}{m}$). Depending on the G_z interval of each ROI, the best compensation varies with TE for the proposed approach.

In Figure 3, S_{norm} and F_{z-shim} are plotted as a function of the TE for three different slices. In each slice, the values were averaged within ROIs of different G_z interval. Similar to Figure 2, with the global approach, the best signal rephasing is achieved when $\overline{G_c} \approx -G_z \approx -100\mu T/m$ (Figure 3B). In contrast, with the proposed approach the signal is gradually rephased for all slices for each block of compensation gradients ($\overline{G_c}^{+}[n = 18, 21, 24] = 0$). Compared with the global approach, the estimated $\overline{G_c}[n]$ for the depicted slices were $\overline{G_c}[18] = -55\mu\frac{T}{m}$, $\overline{G_c}[21] = -105\mu\frac{T}{m}$, and $\overline{G_c}[24] = -175\mu\frac{T}{m}$, which are close to the range of G_z values within the ROIs. Therefore, after each fifth compensation gradient, the signal is nearly ideally compensated in each block. This is indicated when comparing S_{norm} of the echoes $TE_9 = 39.7ms$ and $TE_{15} = 71.9ms$ with F_{z-shim}. Here, the dephasing functions $F_{z-shim} \approx 1$ suggesting an ideal compensation of G_z. Furthermore, when comparing S_{norm} between the slices, S_{norm} is approximately equal for these echoes independent of G_z.

Figure 4 shows the estimated G_z map (Figure 4A) and the obtained R_2^* maps (Figure 4B-F). The R_2^* map from the monoexponential fit of the standard spoiled mGRE (Figure 4B) reveals a strong overestimation proportional to $|G_z|$, which can be drastically decreased by accounting for G_z in the signal model (Figure 4C). Nonetheless, compared with the R_2^* value of 6.4 s^{-1} in the center of the phantom (G_z is close to zero), R_2^* becomes underestimated with increasing $|G_z|$. Applying a global z-shim ($|\overline{G_c}^{+/-}| = 100\mu T/m$) improves the results, especially in areas with $|G_z|$ around $100\mu T/m$ (Figure 4D, slices 5 and 20). Figure 4E demonstrates that the proposed slice-specific approach yields more homogenous R_2^* maps over a wide range of G_z values (eg, slices 2 and 23).

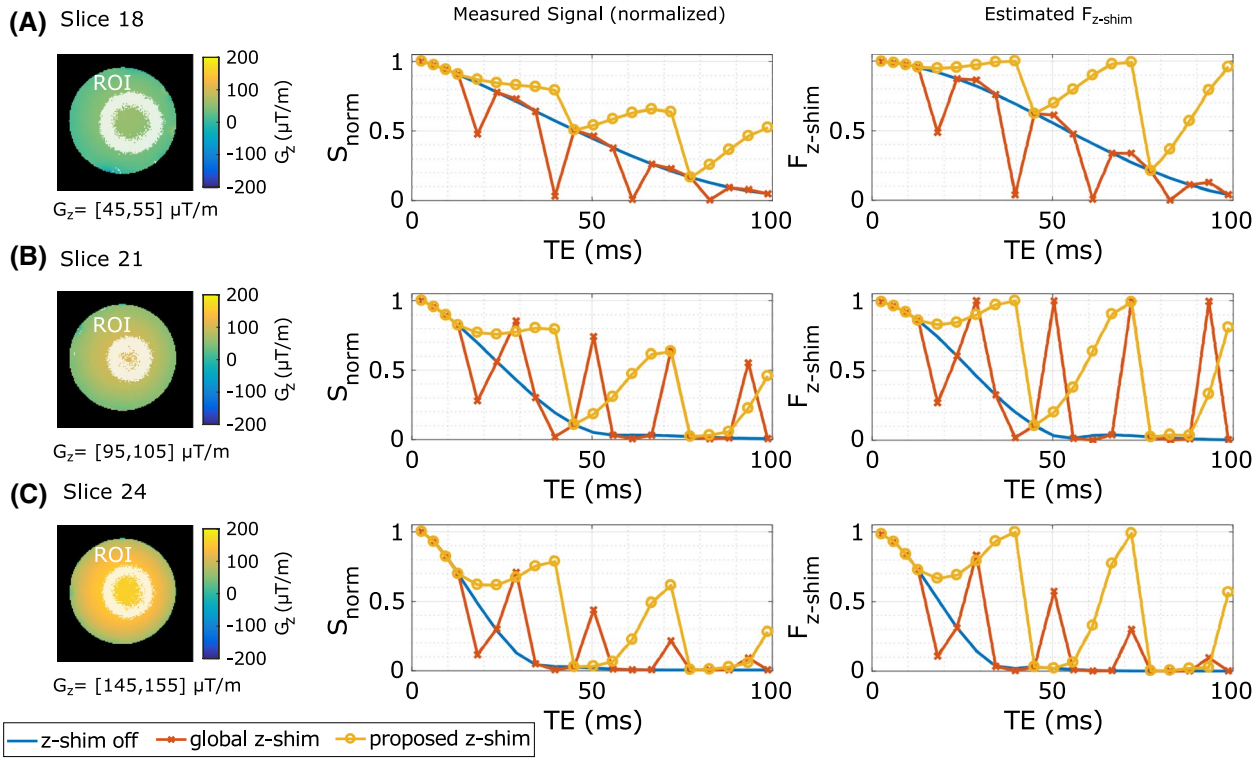

FIGURE 3 Comparison of the measured averaged normalized $S_{norm}\left(TE_i\right)=S\left(TE_i\right)/S\left(TE_1\right)$ (middle) and the averaged estimated dephasing functions $F_{z-shim}\left(TE\right)$ (right) in three slices (A, B, and C). In each slice, averaging was performed in a ROI defined by different intervals of field gradients G_z (left). The lines in the plots show the results from a spoiled mGRE sequence without z-shim gradients in blue, with the global z-shim approach ($|\overline{G}_c^{+/-}|=100\mu T/m$) in red, and with the proposed slice-specific z-shimming in yellow. Note: The interpolation between echoes is solely for illustration purposes

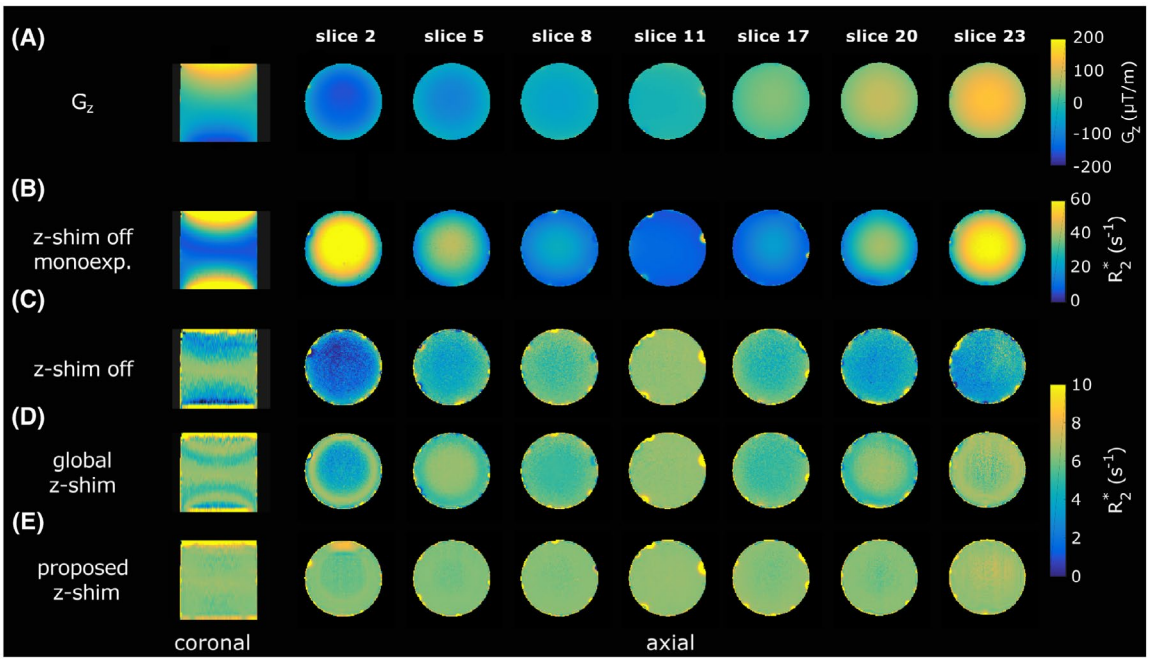

FIGURE 4 Comparison of estimated R_2^* maps of a homogenous phantom. A, The field gradient map G_z. B, The R_2^* maps were calculated from the spoiled mGRE data by assuming a mono-exponential signal model neglecting G_z ($F_{z-shim}=1$). The other R_2^* maps were calculated with the proposed signal model using the data of the spoiled mGRE (C), from the global z-shim ($|\overline{G}_c^{+/-}|=100\mu T/m$) (D), and from the proposed slice-specific approach (E)

Figure 5 shows the averaged R_2^* values of the phantom with a bin size of $G_z = 10\mu\frac{T}{m}$ as a function of G_z, and demonstrates the difference between the proposed approach and the global z-shimming. Although the global z-shim approach ($|\overline{G_c}^{+/-}| = 100\mu\frac{T}{m}$) corrects R_2^* values at about $|G_z| = 100\mu\frac{T}{m}$ to the expected value of 6.4 s^{-1} (R_2^* value at $G_z \approx 0\mu\frac{T}{m}$), the proposed approach yields constant R_2^* values over a broad range of G_z from $-150\mu\frac{T}{m}$ to $125\mu\frac{T}{m}$. Furthermore, the results from the mono-exponential fit of the standard spoiled mGRE data clearly show the strong increase of R_2^* with $|G_z|$.

3.2 | In vivo

Figure 6 shows representative mGRE images for the three investigated sequences (12th to 16th echo). For the spoiled mGRE sequence (Figure 6A), a faster signal decay in areas with strong G_z, for example, close to the nasal cavities, can be observed. For all sequences, the 12th echo images as well as the 16th echo images are equal because of a zero net moment ($M_{c,12} = 0$ and $M_{c,16} = 0$). Between these two echoes, the signal in various brain areas is differently rephased and dephased, depending on the z-shim approach and G_z. The global z-shim pattern with $|\overline{G_c}^{+/-}| = 220\mu T/m$ shows that negative G_z values and positive G_z values are rephased at the 13th and 15th, respectively (Figure 6B). Instead of single positive and negative G_z, a larger range of G_z values can be covered by the proposed approach (Figure 6C) (red arrows).

The R_2^* maps in Figure 7 demonstrate improvements in areas with strong G_z from the global z-shim pattern using constant $|\overline{G_c}^{+/-}| = 220\mu T/m$ (Figure 7C) over the spoiled mGRE (Figure 7A,B), which are most pronounced in the temporal

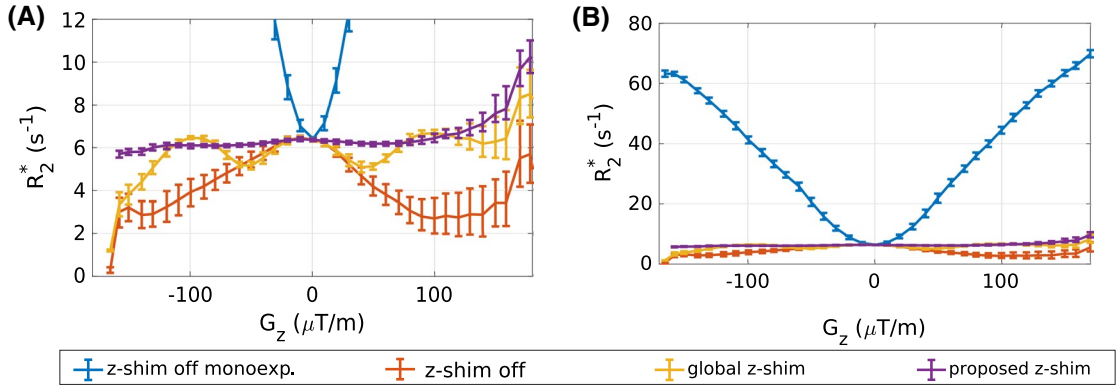

FIGURE 5 A,B, The R_2^* values obtained from the phantom experiments as a function of the field gradient G_z (bin size = 10 μT/m) with different scaling of the R_2^* axes . From the spoiled mGRE data, R_2^* values were first estimated assuming a mono-exponential signal model (blue line) neglecting G_z ($F_{z-shim} = 1$), and second by using the proposed model (red line). Furthermore, R_2^* values from the global z-shim approach ($|\overline{G_c}^{+/-}| = 100\mu\frac{T}{m}$) (yellow) and the proposed slice-specific method (purple) are plotted. The R_2^* values are shown as median and 25th and 75th percentiles (whiskers)

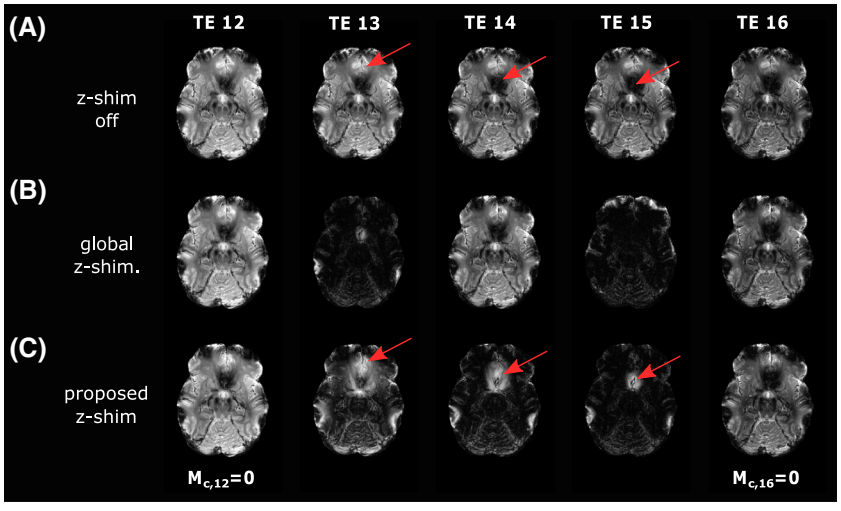

FIGURE 6 Last five GRE images from TE_{12} to TE_{16} acquired with a spoiled mGRE sequence without z-shimming (A), with the global z-shim (B), and with the proposed slice-specific z-shimming approach (C). At TE_{12} as well as at TE_{16}, the sum of the compensation moments ($M_{c,12}$, $M_{c,16}$) is zero for all sequences. With the proposed approach, the signal can also be rephased in areas where it has already been completely dephased (arrows). The complete series of the echoes with z-shim gradients is illustrated in Supporting Information Figure S2

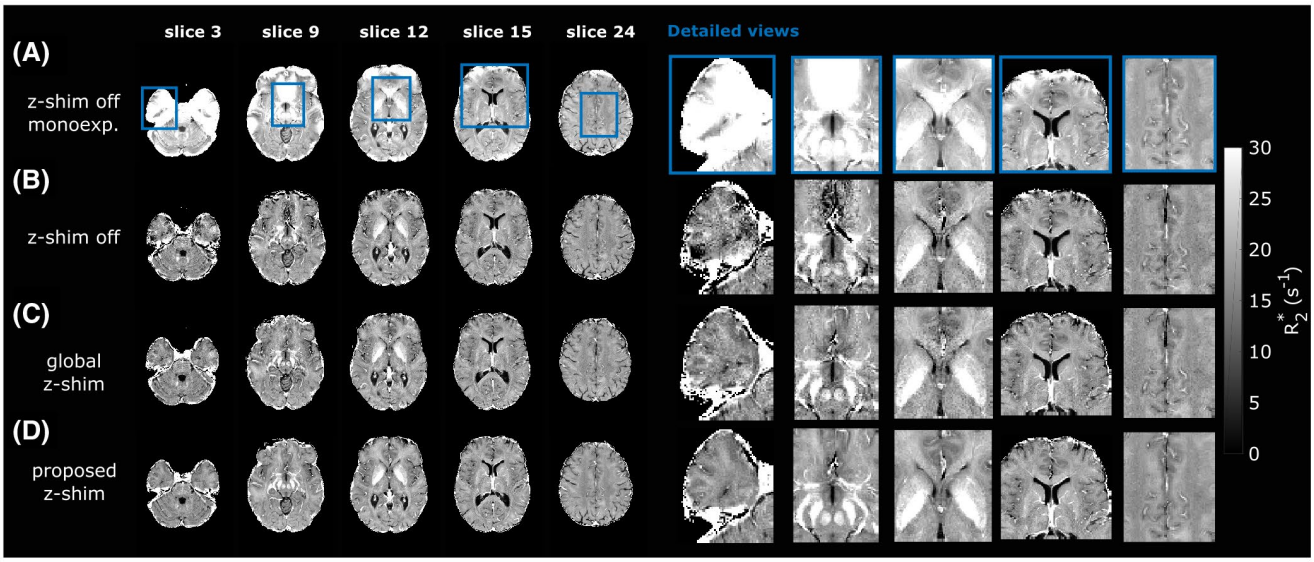

FIGURE 7 Axial views of estimated in vivo R_2^* maps (left), with detailed views of the blue rectangular regions (right). A, The R_2^* maps were directly calculated from the spoiled mGRE data by assuming a mono-exponential signal model neglecting G_z ($F_{z-shim} = 1$). The other R_2^* maps were calculated using the proposed signal model for the spoiled mGRE (B), the global z-shim ($|\overline{G}_c^{+/-}| = 220\mu T/m$) (C), and the proposed slice-specific approach (D) data. An increase in SNR can be observed from (C) to (D) due to higher signal recovery

TABLE 2 Regional R_2^* (s^{-1}) obtained with the four evaluated approaches in three subjects

	Method	Global WM	Caudate nucleus	Globus pallidus	Putamen	Thalamus	Brainstem
Subject 1 (m, 33 years)	Z-shim off monexp.	22.12 (4.26)	20.87 (3.97)	40.34 (8.33)	25.49 (5.11)	23.44 (3.47)	25.91 (6.88)
	Z-shim off	19.25 (3.31)	19.77 (3.17)	36.03 (8.55)	22.74 (4.06)	19.96 (3.78)	16.99 (7.07)
	Global z-shim	19.20 (3.19)	19.62 (2.96)	36.05 (8.09)	22.73 (4.16)	19.87 (3.71)	17.07 (5.93)
	Proposed z-shim	19.20 (2.92)	19.74 (2.95)	35.98 (7.34)	22.77 (3.85)	19.89 (3.29)	17.80 (3.76)
Subject 2 (m, 30 years)	Z-shim off monexp.	23.74 (4.89)	22.37 (3.93)	38.30 (6.55)	28.55 (5.99)	26.05 (3.66)	25.40 (5.65)
	Z-shim off	18.75 (3.65)	19.85 (3.31)	31.50 (6.91)	22.33 (4.53)	18.87 (4.89)	17.01 (5.96)
	Global z-shim	18.81 (3.47)	19.72 (3.09)	31.26 (6.30)	21.97 (4.32)	18.77 (4.30)	16.81 (5.67)
	Proposed z-shim	18.84 (3.05)	19.78 (2.84)	31.78 (5.75)	22.34 (4.08)	18.93 (3.75)	17.41 (3.96)
Subject 3 (m, 51 years)	Z-shim off monexp.	22.12 (4.87)	23.88 (5.17)	40.74 (14.08)	29.64 (7.31)	22.95 (4.15)	31.67 (12.46)
	Z-shim off	19.56 (3.58)	22.35 (3.89)	37.87 (14.98)	27.10 (6.73)	20.60 (3.94)	18.22 (7.87)
	Global z-shim	19.60 (3.44)	22.12 (3.32)	37.35 (14.27)	27.12 (6.26)	20.53 (3.79)	18.60 (5.81)
	Proposed z-shim	19.73 (3.22)	22.14 (3.83)	37.38 (13.73)	27.12 (6.18)	20.86 (3.81)	18.69 (4.40)

Note: Data are presented as median (interquartile range).

Abbreviations: GM, gray matter; m, male; monexp., mono-exponential; WM, white matter.

lobe and cerebellum (slice 3) or close to the sinuses (slice 9). Further improvements and additionally increased SNR are observed in the R_2^* maps obtained with the proposed adaptive z-shim (Figure 7D).

Table 2 summarizes global and regional R_2^* values for all subjects. In line with the visual assessment in Figure 7, the interquartile ranges are smallest for the proposed approach in white matter, followed by the global z-shim method. The largest interquartile ranges were obtained without z-shimming and when assuming a mono-exponential signal model.

4 | DISCUSSION

We have introduced an adaptive slice-specific z-shimming approach that allows one to minimize effects of macroscopic field gradients in the slice-selection direction in 2D mGRE sequences. For each slice n, a maximum positive and negative compensation gradient $\overline{G}_c^{+/-}[n]$ is obtained from a fast prescan. To increase the coverage of compensated G_z values, $\overline{G}_c^{+/-}[n]$ is split into three fractions: $\left(\left[\frac{1}{3}, \frac{2}{3}, \frac{3}{3}\right]\overline{G}_c^{+/-}[n]\right)$.

Based on these gradient values, a pattern of compensation moments between the echoes is calculated (Figure 1C).

Our novel adaptive slice-specific z-shimming was compared with a conventional spoiled mGRE sequence and a global z-shimming approach that applies a positive and negative $\overline{G}_c^{+/-}$ (Figure 1B) independent of the slice position.[31,32] In contrast to modeling of the standard spoiled mGRE, the global z-shim enables us to recover R_2^* values in areas with strong G_z, which is in line with the results of Nam et al.[31] By performing slice-specific z-shimming with more compensated G_z values, the proposed approach results in SNR improvements (Figure 7). Quantitatively, the measured values are within the range of reported values in the literature at 3 T. The z-shim approach by Nam et al yielded an R_2^* of 20.77 s^{-1} for the putamen and 34.22 s^{-1} for the globus pallidus,[31] which is close to the mean values of our 3 subjects with 24.08 s^{-1} and 35.05 s^{-1}. When considering the age of the subjects, our R_2^* values are in good agreement with a study reporting different age ranges.[45] Subjects' regional R_2^* values in the caudate nucleus, thalamus, and brainstem are within the 95% confidence interval of this study.[45] For subjects 1 and 3, the R_2^* values in the globus pallidus are slightly above the 95% confidence interval as well as in the putamen for subject 3. For example, in the putamen of subject 3 (51 years), R_2^* is 27.12 s^{-1} compared with Sedlacik et al, who reported an R_2^* of 24.3 (22.1 − 26.6) s^{-1}.[45]

During the optimization process of selecting the optimal $\overline{G}_c^{+/-}[n]$ from the prescan field gradient map $G_{z,pre}[n]$, splitting of the compensation gradients into different magnitudes was performed. When using a single value (eg, maximum and minimum of positive and negative $G_{z,pre}[n]$), improvements were only observed in areas with G_z values close to the specific compensation gradient. To demonstrate this relation, additional measurements with a slice-specific approach but with a single $\overline{G}_c^{+/-}[n]$ were performed. As shown in Supporting Information Figure S1, splitting $\overline{G}_c^{+/-}[n]$ led to a more robust compensation over a wide range of G_z values. A further refinement of our approach could be made by passing the desired compensation gradient for each echo $\overline{G}_c^{+/-}[n, TE_i]$ to the sequence. This comes with the advantage that the compensation gradients can be individually selected, based on the distribution of G_z values in each slice.

Z-shim approaches primarily aim to avoid signal dephasing in areas with large G_z. In this context, a rather unexpected finding was that also areas with relatively low field gradients ($|G_z| < 50\mu T/m$) yielded higher SNR in R_2^* maps by applying small compensation gradients compared with postprocessing-only methods (Figure 7, slice 24). This SNR increase might be especially promising for combined applications with acceleration methods such as parallel imaging[46,4748]

The proposed approach has some limitations. First, a prescan with a duration of 15 seconds is necessary to estimate G_z. However, this additional scan time is minimal compared with the fully sampled z-shim acquisition (7 minutes 20 seconds) itself, and the increase in SNR compensates for the prolonged scan time. Another issue, especially in vivo, is the estimation of a reliable field gradient $G_z| < 50\mu T/m$ map from the prescan, which is used to define R_2^*. Here, we focused on a robust implementation and avoided potential gradient errors due to missing field-map values in the skull by eroding the $\overline{G}_c^{+/-}[n]$ map. Nevertheless, it might result in nonoptimal compensation gradients in these areas. An alternative might be to match the slice position to a template G_z map instead of performing a prescan.[49]

This work focuses on z-shimming because the signal dephasing is major along the slice-selective (z-)direction compared with the orthogonal directions. In addition, strong in-plane field gradients can be considered by calculating additional compensation moments in in-plane directions or, as proposed by Yablonskiy et al,[50] by modeling the signal dephasing with the voxel spread function.

We have recently introduced a signal modeling approach for an arbitrary excitation pulse and $^{F_{z-shim}}$,[23] which has been adapted in the current work to describe signal dephasing F_{z-shim} due to G_z and the compensation gradient $\overline{G}_c$. Because R_2^* is estimated from the measured data by nonlinear fitting of Equation (2), any modeling error in F_{z-shim} will propagate into the R_2^* estimate. Here, B_1^+ and λ have been considered for modeling, but additionally, the ratio TR/T_1 can affect F_{z-shim}. If the assumption $TR \gg T_1$ is not fulfilled, $\underline{M}_{xy}(z)$ changes according to the steady-state equation for spoiled gradient-echo sequences[51] and might bias F_{z-shim}. To better assess the contributions of B_1^+, λ, and TR/T_1 to F_{z-shim}, additional simulations were carried out for different G_z values (Supporting Information Figure S3). For a ratio of $TR/T_1 = 5$, T_1 effects are negligibly small, while errors due to B_1^+ increase with α. Compared with B_1^+, the estimated errors caused by λ are similar for each α. In contrast, for $TR/T_1 = 2$, a T_1 bias can be observed, which is small compared with the B_1^+ error. To investigate the influence of B_1^+ and λ in vivo, Supporting Information Table S1 lists the results without considering B_1^+ and λ. It reveals that the greatest relative change of R_2^* for the proposed approach was 2.7% for subject 3 in the brain stem (Supporting Information Table S2). These small changes in R_2^* suggest that B_1 mapping might not be necessary for the regions evaluated. However, when increasing α or when evaluation regions with stronger G_z, accounting for B_1^+ might be beneficial. Based on the simulation results, a potential small T_1 effect cannot be excluded with the TR = 2.5 seconds used in vivo.

Other sources for model deviations in F_{z-shim} are the input parameters G_z and $\overline{G}_c$. Similar as for the prescan, G_z estimation is challenging if the field map values from adjacent slices are missing. For $\overline{G}_c$, it is assumed that it is ideally characterized by the actual applied gradient moment of the MRI system. Thus, errors might occur in case of gradient imperfections or when a different MRI system is used. In our experiments, a good correspondence between the predicted signal dephasing F_{z-shim} and the measured signal S_{norm} (Figures 2 and 3) was observed, indicating a reasonable accurate $\overline{G}_c$ for the proposed approach.

5 | CONCLUSIONS

A new adaptive slice-specific z-shim approach in combination with signal modeling for 2D mGRE data was introduced to minimize the effects of macroscopic field gradients. The proposed approach allows a more robust correction of R_2^* maps over a broad range of field gradients and additionally provides a higher SNR.

DATA AVAILABILITY STATEMENT

The code and data that support the findings of this study are openly available in R2s mapping at https://github.com/neuroimaging-mug/R2s-mapping.

ORCID

Martin Soellradl https://orcid.org/0000-0002-3760-5578
Johannes Strasser https://orcid.org/0000-0002-2396-5126
Andreas Lesch https://orcid.org/0000-0003-2492-3566
Rudolf Stollberger https://orcid.org/0000-0002-4969-3878
Christian Langkammer https://orcid.org/0000-0002-7097-9707

REFERENCES

1. Ogg RJ, Langston JW, Haacke EM, Steen RG, Taylor JS. The correlation between phase shifts in gradient-echo MR images and regional brain iron concentration. *Magn Reson Imaging*. 1999;17:1141-1148.
2. Li L, Leigh JS. Quantifying arbitrary magnetic susceptibility distributions with MR. *Magn Reson Med*. 2004;51:1077-1082.
3. Liu C. Susceptibility tensor imaging. *Magn Reson Med*. 2010;63:1471-1477.
4. Li TQ, Yao B, Van Gelderen P, et al. Characterization of T2* heterogeneity in human brain white matter. *Magn Reson Med*. 2009;62:1652-1657.
5. Yao B, Li TQ, van Gelderen P, Shmueli K, de Zwart JA, Duyn JH. Susceptibility contrast in high field MRI of human brain as a function of tissue iron content. *Neuroimage*. 2009;44:1259-1266.
6. Haacke EM, Xu Y, Cheng Y-CN, Reichenbach JR. Susceptibility weighted imaging (SWI). *Magn Reson Med*. 2004;52:612-618.
7. Du YP, Chu R, Hwang D, et al. Fast multislice mapping of the myelin water fraction using multicompartment analysis of T2* decay at 3T: A preliminary postmortem study. *Magn Reson Med*. 2007;58:865-870.
8. Hwang D, Kim DH, Du YP. In vivo multi-slice mapping of myelin water content using T2* decay. *Neuroimage*. 2010;52:198-204.
9. Lee J, van Gelderen P, Kuo LW, Merkle H, Silva AC, Duyn JH. T2*-based fiber orientation mapping. *Neuroimage*. 2011;57:225-234.
10. Bender B, Klose U. The in vivo influence of white matter fiber orientation towards B0 on T2* in the human brain. *NMR Biomed*. 2010;23:1071-1076.
11. Van Gelderen P, De Zwart JA, Lee J, Sati P, Reich DS, Duyn JH. Nonexponential T2* decay in white matter. *Magn Reson Med*. 2012;67:110-117.
12. Ulla M, Bonny JM, Ouchchane L, Rieu I, Claise B, Durif F. Is R2* a new MRI biomarker for the progression of Parkinson's disease? A longitudinal follow-up. *PLoS One*. 2013;8:1-8.
13. Walsh AJ, Blevins G, Lebel RM, Seres P, Emery DJ, Wilman AH. Longitudinal MR imaging of iron in multiple sclerosis: An imaging marker of disease. *Radiology*. 2014;270:186-196.
14. Wood JC, Enriquez C, Ghugre N, et al. MRI R2 and R2* mapping accurately estimates hepatic iron concentration in transfusion-dependent thalassemia and sickle cell disease patients. *Blood*. 2005;106:1460-1465.
15. Anderson LJ, Holden S, Davis B, et al. Cardiovascular T2-star (T2*) magnetic resonance for the early diagnosis of myocardial iron overload. *Eur Heart J*. 2001;22:2171-2179.
16. Yablonskiy DA. Quantitation of intrinsic magnetic susceptibility-related effects in a tissue matrix. Phantom study. *Magn Reson Med*. 1998;39:417-428.
17. Young IR, Cox IJ, Bryant DJ, Bydder GM. The benefits of increasing spatial resolution as a means of reducing artifacts due to field inhomogeneities. *Magn Reson Imaging*. 1988;6:585-590.
18. Fernndez-Seara MA, Wehrli FW. Postprocessing technique to correct for background gradients in image-based R_2^* measurements. *Magn Reson Med*. 2000;44:358-366.
19. Dahnke H, Schaeffter T. Limits of detection of SPIO at 3.0 T using T_2^* relaxometry. *Magn Reson Med*. 2005;53:1202-1206.
20. Preibisch C, Volz S, Anti S, Deichmann R. Exponential excitation pulses for improved water content mapping in the presence of background gradients. *Magn Reson Med*. 2008;60:908-916.
21. Yang X, Sammet S, Schmalbrock P, Knopp MV. Postprocessing correction for distortions in T2* decay caused by quadratic cross-slice B0 inhomogeneity. *Magn Reson Med*. 2010;63:1258-1268.
22. Hernando D, Vigen KK, Shimakawa A, Reeder SB. R2* mapping in the presence of macroscopic B0 field variations. *Magn Reson Med*. 2012;68:830-840.
23. Soellradl M, Lesch A, Strasser J, et al. Assessment and correction of macroscopic field variations in 2D spoiled gradient-echo sequences. *Magn Reson Med*. 2020;84:620-633.
24. Frahm J, Merboldt K-D, Hänicke W. Direct FLASH MR imaging of magnetic field inhomogeneities by gradient compensation. *Magn Reson Med*. 1988;6:474-480.
25. Ordidge RJ, Gorell JM, Deniau JC, Knight RA, Helpern JA. Assessment of relative brain iron concentrations using T2-weighted and T2*-weighted MRI at 3 Tesla. *Magn Reson Med*. 1994;32:335-341.
26. Yang QX, Williams GD, Demeure RJ, Mosher TJ, Smith MB. Removal of local field gradient artifacts in T2*-weighted images at

high fields by gradient-echo slice excitation profile imaging. *Magn Reson Med*. 1998;39:402-409.
27. Yang QX, Dardzinski BJ, Demeure RJ, Briggs RW SM. Removal of local field gradient artifacts in T2* measurement and T2* contrast at high field. In: Proceedings of the 6th Annual Meeting of ISMRM, Sydney, Australia, 1998. p 578.
28. Truong TK, Chakeres DW, Scharre DW, Beversdorf DQ, Schmalbrock P. Blipped multi gradient-echo slice excitation profile imaging (bmGESEPI) for fast T2* measurements with macroscopic B0 inhomogeneity compensation. *Magn Reson Med*. 2006;55:1390-1395.
29. Meng Y, Lei H. A single-scan T2* mapping method based on two gradient-echo images with compensation for macroscopic field inhomogeneity. *Magn Reson Med*. 2008;60:1388-1395.
30. Wild JM, Wayne Martin WR, Allen PS. Multiple gradient echo sequence optimized for rapid, single-scan mapping of R2* at high B0. *Magn Reson Med*. 2002;48:867-876.
31. Nam Y, Han D, Kim DH. Single-scan R2* measurement with macroscopic field inhomogeneity correction. *Neuroimage*. 2012;63:1790-1799.
32. Lee D, Lee J, Lee J, Nam Y. Single-scan z-shim method for reducing susceptibility artifacts in gradient echo myelin water imaging. *Magn Reson Med*. 2018;80:1101-1109.
33. Hu X, Kim SG. Reduction of signal fluctuation in functional MRI using navigator echoes. *Magn Reson Med*. 1994;31:495-503.
34. Wen J, Cross AH, Yablonskiy DA. On the role of physiological fluctuations in quantitative gradient echo MRI: Implications for GEPCI, QSM, and SWI. *Magn Reson Med*. 2015;73:195-203.
35. Luo J, Jagadeesan BD, Cross AH, Yablonskiy DA. Gradient echo plural contrast imaging—Signal model and derived contrasts: T2*, T1, Phase, SWI, T1f, FST2*and T2*-SWI. *Neuroimage*. 2012;60:1073-1082.
36. Aigner CS, Clason C, Rund A, Stollberger R. Efficient high-resolution RF pulse design applied to simultaneous multi-slice excitation. *J Magn Reson*. 2016;263:33-44.
37. Reichenbach JR, Venkatesan R, Yablonskiy DA, Thompson MR, Lai S, Haacke EM. Theory and application of static field inhomogeneity effects in gradient-echo imaging. *J Magn Reson Imaging*. 1997;7:266-279.
38. Sacolick LI, Wiesinger F, Hancu I, Vogel MW. B1 mapping by Bloch-Siegert shift. *Magn Reson Med*. 2010;63:1315-1322.
39. Smith SM, Jenkinson M, Woolrich MW, et al. Advances in functional and structural MR image analysis and implementation as FSL. *Neuroimage*. 2004;23(Suppl 1):S208-S219.
40. Lesch A, Schloegl M, Holler M, Bredies K, Stollberger R. Ultrafast 3D Bloch-Siegert B1+-mapping using variational modeling. *Magn Reson Med*. 2019;81:881-892.
41. Smith SM, Zhang Y, Jenkinson M, et al. Accurate, robust, and automated longitudinal and cross-sectional brain change analysis. *Neuroimage*. 2002;17:479-489.
42. Patenaude B, Smith SM, Kennedy DN, Jenkinson M. A Bayesian model of shape and appearance for subcortical brain segmentation. *Neuroimage*. 2011;56:907-922.
43. Jenkinson M, Smith S. A global optimisation method for robust affine registration of brain images. *Med Image Anal*. 2001;5:143-156.
44. Jenkinson M, Bannister P, Brady M, Smith S. Improved optimization for the robust and accurate linear registration and motion correction of brain images. *Neuroimage*. 2002;17:825-841.
45. Sedlacik J, Boelmans K, Löbel U, Holst B, Siemonsen S, Fiehler J. Reversible, irreversible and effective transverse relaxation rates in normal aging brain at 3T. *Neuroimage*. 2014;84:1032-1041.
46. Pruessmann KP, Weiger M, Scheidegger MB, Boesiger P. SENSE: Sensitivity encoding for fast MRI. *Magn Reson Med*. 1999;42:952-962.
47. Griswold MA, Jakob PM, Heidemann RM, et al. Generalized autocalibrating partially parallel acquisitions (GRAPPA). *Magn Reson Med*. 2002;47:1202-1210.
48. Breuer FA, Blaimer M, Mueller MF, et al. Controlled aliasing in volumetric parallel imaging (2D CAIPIRINHA). *Magn Reson Med*. 2006;55:549-556.
49. Volz S, Callaghan MF, Josephs O, Weiskopf N. Maximising BOLD sensitivity through automated EPI protocol optimisation. *Neuroimage*. 2019;189:159-170.
50. Yablonskiy DA, Sukstanskii AL, Luo J, Wang X. Voxel spread function method for correction of magnetic field inhomogeneity effects in quantitative gradient-echo-based MRI. *Magn Reson Med*. 2013;70:1283-1292.
51. Ernst RR, Anderson WA. Application of Fourier transform spectroscopy to magnetic resonance. *Rev Sci Instrum*. 1966;37:93-102.

SUPPORTING INFORMATION

Additional Supporting Information may be found online in the Supporting Information section.

FIGURE S1 Phantom results obtained when extending the global z-shim pattern (Figure 1B) by a slice-specific (intermediate) pattern. A, The magnitude images from TE_{10} to TE_{20}. B, The R_2^* maps. The differences of the methods in two regions of interest (ROIs) with different mean G_z (C) are assessed by comparing the measured signal decays (D). While with the estimated single $\overline{G_c}\,[n] = -115\mu\frac{T}{m}$, a nearly ideal compensation can be achieved when $\overline{G_c}\,[n] \approx -G_z$ (ROI 1), in the case of heterogeneous G_z values, a more robust compensation can be achieved when fractioning $\overline{G_c}\,[n]$ (ROI 2). Note: The interpolation between echoes is solely for illustration purposes

FIGURE S2 Gradient-echo images from TE_4 to TE_{16} acquired with a spoiled multi-echo gradient-echo (mGRE) sequence without z-shimming (A), with the global z-shim (B), and with the proposed slice-specific z-shimming approach (C). At TE_4, TE_8, TE_{12}, and TE_{16}, the sum of the compensation moments $M_{c,4}$, $M_{c,8}$, $M_{c,12}$, and $M_{c,16}$ is zero for all sequences. With the proposed approach, the signal can also be rephased in areas where it has been already completely dephased (arrows)

FIGURE S3 Simulation results for studying the sensitivity of variations in α due to B_1^+, spatial broadening or narrowing of $\underline{M}_{xy}$ with factor $\lambda = \frac{G_{slice}}{G_{slice}+G_z}$, and incomplete T_1 relaxation for R_2^* estimation. The plots show the relative error (%) of R_2^* as a function of G_z, estimated from forward simulation of the

signal decay with a reference model, which includes B_1^+, λ, and TR/T_1. While neglecting TR/T_1, the error was obtained with and without considering B_1^+ and λ for modeling F_{z-shim} for each parameter combination. In the reference model, the flip angle was scaled with a factor $\xi = [0.6, 0.8, 1, 1.2, 1.4]$ to simulate B_1^+ variations ($\alpha_{sim} = \alpha\xi$). Then, the spatial coordinates along the slice direction were scaled with λ, and to account for the T_1 relaxation effects, $\underline{M}_{xy}$ was calculated with the steady-state equation for spoiled gradient-echo (GRE) sequences for $TR/T_1 = 2$ and $TR/T_1 = 5$. Simulations were carried out with the same TEs and excitation pulse as used in the in vivo measurements, and $R_2^* = 30s^{-1}$ was assumed. For $TR/T_1 = 5$, the relative error is negligible when including B_1^+ and λ for all simulated flip angles, because of complete T_1 relaxation. Thus, T_1 influence can be neglected. Without B_1^+ and λ, for $\alpha = 30°$, the error is relatively small and driven primarily by λ. For larger α, the B_1^+ related error increases and becomes the dominant factor. Compared with $\alpha = 90°$, for $\alpha = 60°$ the relative error is smaller than 10% over a wide range of $\boldsymbol{G}_z$ and ξ. In contrast, for $TR/T1 = 2$, substantial errors due to incomplete T_1 relaxation can be observed in both models

TABLE S1 Regional $R_2^*\left(s^{-1}\right)$ presented as median (interquartile range) obtained with the four evaluated methods in 3 subjects. Note: Values were estimated without including variations of the nominal flip angle due to B_1^+ and spatial broadening or narrowing of $\underline{M}_{xy}$ with λ caused by the supposition of $\boldsymbol{G}_z$ and $\boldsymbol{G}_{slice}$ in the model for Equation (2)

TABLE S2 Relative change (%) of $R_2^*\left(s^{-1}\right)$ values estimated with (Table 2) and without including B_1^+ and $\boldsymbol{\lambda}$ variations (Supporting Information Table S1) for modeling F_{z-shim}

How to cite this article: Soellradl M, Strasser J, Lesch A, Stollberger R, Ropele S, Langkammer C. Adaptive slice-specific z-shimming for 2D spoiled gradient-echo sequences. *Magn Reson Med*. 2021;85:818–830. https://doi.org/10.1002/mrm.28468